sciendo

ISSN 1335-8871

MEASUREMENT SCIENCE REVIEW

Journal homepage: https://content.sciendo.com

In vivo Volumetric, DTI and ^{1}H MRS Rat Brain Protocol for Monitoring Early Neurodegeneration and Efficacy of the Used Therapy

Tomáš Tvrdík[1,2], Ľubomír Melicherčík[1,2], Katarína Šebeková[3], Jakub Szabó[3], Marianna Maková[1], Daniel Gogola[4], Svatava Kašparová[1*]

[1]*Central Laboratories, Faculty of Chemical and Food Technology, Slovak University of Technology in Bratislava, Radlinského 9, 81237, Bratislava, Slovakia, ttvrdik@prodiagnostic.sk, lmelichercik@prodiagnostic.sk, marianna.makova@stuba.sk, ladislav.baciak@stuba.sk, svatava.kasparova@stuba.sk*

[2]*Department of Radiology, Faculty of Medicine of Comenius University in Bratislava, Slovak Medical University and University Hospital Bratislava, Mickiewiczova 13, 81369 Bratislava, Slovakia*

[3]*Institute of Molecular Biomedicine, Faculty of Medicine of Comenius University in Bratislava, Sasinkova 4, 81108, Bratislava, Slovakia, katarina.sebekova@imbm.sk, jakub.szabo@imbm.sk*

[4]*Institute of Measurement Science, Slovak Academy of Sciences, Dúbravská cesta 9, 841 04 Bratislava, Slovakia, daniel.gogola@savba.sk*

Abstract: The aim of our study was to develop a multimodal experimental protocol for *in vivo* imaging and metabolic parameters (MRI, DTI and ^{1}H MRS) in an animal model of neurodegeneration. We have successfully developed the protocol for simultaneous DTI/MRI/^{1}H MRS measurement to ensure unaltered conditions for repeatable non-invasive experiments. In this experiment, diffusion tensor imaging, spectroscopic and volumetric "bio-markers" were generated in the brain for the D-galactose model of "age-related dementia". The hippocampal relative volume, taurine and myo-inositol relative concentrations were found to be significant predictors contributing to the differences between the groups of rats treated with D-galactose in simulated "neurodegeneration", even in response to the applied Huperzine A therapy.

Keywords: Animals, multimodal imaging, *in vivo*, diffusion tensor imaging (DTI), magnetic resonance spectroscopy (MRS).

1. INTRODUCTION

The aim of our study was to advance the technical possibilities in preclinical research of neurodegeneration in animal models. We designed and optimised a multimodal experiment in which it would be possible to measure and compare several magnetic resonance imaging (MRI), diffusion tensor imaging (DTI) and proton magnetic resonance spectroscopic (^{1}H MRS) parameters of small animal brains, with all parameters studied being acquired in one measurement session. These parameters would diagnose the early stages of neurodegeneration and reflect the evaluated neuroprotective therapeutic effect of a drug. Using simultaneous multimodal *in vivo* measurements, we provided unaltered experimental conditions that would not be affected by repeated anaesthesia. Before animals were randomly assigned to experimental groups, baseline structural, microscopic and metabolic parameters were measured in all animals. These data could then be compared for each animal throughout the experiment.

For the pilot study, we chose the non-genetic model of neurodegeneration using the metabolic effects of D-galactose (D-Gal) overdose in adult Wistar rats [1]. We compared the hippocampal regions, as well as selected white matter structures, to determine which of the measured parameters would have the best validity for detecting the early stages of neurodegeneration while reflecting the disease-modifying effects of neuroprotective therapy with Huperzine A (HupA) [2], [3].

Neurodegenerative diseases associated with dementia are a serious socioeconomic and medical problem [4]. These diseases usually develop over a long period of time. Despite advances in diagnostic imaging, it is difficult to diagnose them in the early stages before the onset of irreversible brain atrophy [5], [6]. Non-hereditary forms of dementia are known to be related to ageing. Animal models simulating brain ageing and incipient dementia, in conjunction with modern non-invasive MR techniques, play a significant role in this research. By exploring and searching for the most viable

DOI: 10.2478/msr-2023-0030

*Corresponding author: svatava.kasparova@stuba.sk (S. Kašparová)

markers in MRI of suitable pathophysiological animal models, we can successfully simulate and validate such neurodegeneration.

MRI or computed tomography (CT) imaging of advanced stages of Alzheimer's disease can detect structural changes in the grey matter of the medial temporal lobe, hippocampus and associated white matter [7]. Volumetry of these regions is a readily available method to evaluate atrophy. Semi-quantitative evaluation of medial temporal lobe atrophy can assess disease progression [8]. However, atrophy in these regions is also specific to other types of dementia, and volumetry supports differentiation of other possible causes of dementia [9]. Molecular imaging methods, such as positron emission tomography can reveal hypometabolism in the affected areas of the brain [10]. Both qualitative and quantitative information on metabolic changes in grey matter are well documented and can be studied using *in vivo* localised ^{1}H MR spectroscopy (MRS) [11]. The explanation of the white matter degeneration mechanisms in Alzheimer's disease is currently not as detailed as of grey matter changes. Apart from secondary white matter damage through the mechanisms of Wallerian degeneration [12], there is also primary white matter damage. In the early stages of Alzheimer's disease, white matter damage may be partially independent of grey matter changes [13]. Diffusion MRI imaging offers the possibility of a non-invasive measurement of the microarchitectural properties of living tissue. The measured data can be fitted to various models based on more or less simplified assumptions about white matter microstructure. One of the simplest but widely used models is DTI [14], [15], [16], which generates four diffusion indices for each measured voxel: fractional anisotropy (FA), mean diffusivity (MD), radial diffusivity (RD), axial diffusivity (AD) [17]. These data quantify diffusion and its anisotropy in the whole voxel, where several populations of crossing white matter tracts are usually present [18]; therefore, we should interpret the results with caution [19].

The distinction between normal deterioration of cognitive functions caused by physiological ageing and pathological changes in neurodegenerative processes is crucial for planning possible treatment strategies. There is a suggestion that memory disruption, most prominent in elderly people, is partially supported by ageing processes [20]. There is a long-established link between mild cognitive impairment (MCI) and Alzheimer's disease, the most common form of dementia. People diagnosed with MCI are more likely to progress to Alzheimer's form of dementia [6]. Although extensive work has been done to study the pathological changes in the human brain, the early changes that are the background for MCI are difficult to diagnose. The diagnosis of Alzheimer's disease is mainly made through a variety of cognitive and psychological tests. Non-invasive imaging methods of evaluating these processes are available, but they lack specificity when used alone and are mainly used to rule out other treatable causes of symptoms and to track the disease progression [5].

Preclinical studies in animals have shown that chronic administration of high doses of D-Gal is a widely used model for ageing and neurodegeneration in small rodents based on an alternative biochemical pathway producing galactitol and galactonate [1], [21]. Mechanisms of D-Gal overdose include oxidative stress, a pro-inflammatory state and energetic metabolism changes in the hippocampus; the pathological changes are similar to sporadic Alzheimer's disease [22], [23], [24], [25]. The D-Gal model, which simulates the ageing of brain structures, has not yet been studied with regard to tractographic parameters; therefore, this relatively demanding MR method has been included in our multimodal experiment. We wanted to find out, for example, whether the pre-inflammatory conditions in the brain caused by D-Gal are reflected in the tractographic and DTI parameters and simultaneously correlated with the increase in myo-Inositol in the metabolic profile of the hippocampus.

HupA is a selective, reversible inhibitor of acetylcholinesterase (AChE) and N-methyl-D-aspartate (NMDA) receptor antagonist. It has shown anti-apoptotic and anti-inflammatory properties that have been explored for potential benefit in the therapy of neurodegenerative diseases [2], [3].

The pathophysiological mechanisms of the sporadic Alzheimer's disease are not well understood, and causal therapy is currently unavailable. AChE inhibitors in combination with memantine may slow the neurodegeneration progression in moderate and severe Alzheimer's disease [26]. The aim of the presented study was to implement multimodal MR methods to compare them and find the most suitable biomarkers for evaluating neurodegenerative diseases. In this case, we used a model of age-related dementia by daily D-Gal administration. Non-invasive imaging methods can provide helpful information for diagnosing disease in the preclinical stage of the disease and testing the disease-modifying effect of therapy.

2. SUBJECT & METHODS

D-Gal and HupA (Sigma-Aldrich, Germany) were dissolved in saline (B.Braun Melsungen AG, Germany) at concentrations of 100 mg/ml and 30 μg/ml, respectively. The administered daily dose of D-Gal was 300 mg per 1 kg of body weight, the daily dose of HupA was 0.1 mg per 1 kg of body weight.

Four-month-old male Wistar rats (n = 22) (The Department of Toxicology and Laboratory Animal Breeding, Slovak Academy of Sciences, Dobrá Voda, Slovakia) weighing 300-380 g were kept under standard laboratory conditions (temperature 22 ± 2 °C, 45-65 % relative humidity, 12/12 hour light/dark cycle) with unlimited supply of water and food. Animals were housed in groups of four in clear plastic cages. We randomly divided the animals into three experimental groups:

- (one) control group (n = 6),
- (two) D-Gal group (n = 8),
- (three) group treated with HupA and D-Gal simultaneously (n = 8).

All groups received daily subcutaneous injections of saline (group 1), 300 mg/kg D-Gal (group 2), 300 mg/kg D-Gal + 0.1 mg/kg HupA (group 3) throughout the duration of the experiment. Two consecutive *in vivo* MRI/MRS measurements were performed in each of the animals on days 1-9 (baseline) and days 55-58 (second measurement) after the treatment commenced.

Animals were anaesthetised with a short inhalation of 5% isoflurane in air (Forane, Abbvie, USA) and then held in the magnet, inhaling approx. 2% isoflurane in air during scanning. Animals were restrained in the prone position with a tooth bar and nose mask.

The actual dose was adjusted by monitoring respiratory rate with a MR compatible monitoring and gating system (Small Animal Instruments Inc., USA) to maintain 40-50 breaths per minute. We monitored and maintained body temperature by the air heater blowing into the gantry (Small Animal Instruments Inc., USA). According to regulations, all animals were sacrificed by decapitation after the measurements. This study was approved by the State Veterinary and Food Administration of the Slovak Republic (Ro-990/16-221). The health status and weight gain of the animals were checked periodically.

In vivo MRI and ^{1}H MRS measurements were performed on a 4.7 T horizontal magnet with a bore diameter of 12.5 cm and a 400 mT/m gradient insert interfaced to a Direct Drive console (Agilent Technologies, Yarnton, UK), which was equipped with a head holder, a quadrature volume excitation RF coil with an internal diameter of 72 mm (Rapid Biomedical, Rimpar, Germany) and a dual-channel surface receiver coil (Rapid Biomedical, Rimpar, Germany).

DTI and MRI volumetry: Data were acquired together with a diffusion-weighted sequence; volumetric images were then extracted from b = 0 scans, which were equivalent to the T_2-weighted images. After acquisition of gradient echo (GRE) scout images, animal placement corrections and manual shimming for 50% linewidth below 50 Hz, we measured 30 consecutive 0.4 mm thick horizontal diffusion-weighted fast spin-echo slices positioned over telencephalon and brainstem (FOV 38.4×38.4 mm^2, matrix 96×96, TR = 3735 ms, TE_{eff} = 38 ms, echo train length = 8, 8 averages). The in-plane resolution of the diffusion-weighted images was 0.4×0.4 mm^2. (b = 1097 s/mm^2, trapezoidal gradient lobes, G = 150 mT/m, δ = 5 ms, Δ = 26 ms). The x, y, z gradient amplitudes of the 10 non-collinear diffusion-weighted images in half-sphere scheme and the two non-weighted images were [0.80, 0.50, -0.33], [0.97, -0.25, 0.02], [0.32, 0.94, 0.11], [0, 0, 0], [0.11, -0.90, 0.42], [0.10, 0.43, 0.90], [0.77, 0.40, 0.49], [0.63, -0.20, -0.75], [0.61, -0.35, 0.71], [0, 0, 0], [0.50, -0.83, -0.26], [0.21, 0.47, -0.86] in fractions of 150 mT/m. The data were zero-filled to a 128×128 matrix and smoothed in the time domain using the Gaussian filter with constant gf = 0.003 s in both the read and phase directions (VnmrJ 3.1c, Agilent Technologies, Yarnton, UK). The total Fast Spin-Echo (FSE) DTI scan time was just under 54 minutes.

Localised ^{1}H MRS in the right hippocampus of rat brain: We acquired T_2-weighted Fast Spin-Echo Multi-Slice (FSEMS) axial images (15 slices, matrix 256×256, slice thickness = 1 mm, 10 averages) (total scanning time 2 min). These images were used for proper selection of the volume of interest (voxel) for localised *in vivo* ^{1}H MRS in the area of the dorsal part of the right hippocampus with the same coil setup (voxel = 3×3×4 mm^3) as shown in Fig. 1(a). After automatic FASTMAP [27] shimming to achieve a spectral linewidth of < 10 Hz and water suppression calibration (VAPOR sequence) [28], MRS was acquired using the SPECIAL sequence [29] with outer volume suppression (35 mm thickness), TR = 3000 ms, TE = 4.47 ms, TM = 6.30 ms, 8 blocks of 64 dual-channel acquisitions. We performed two measurements of the unsuppressed water used as an internal reference for calculating the absolute concentrations of the metabolites. The *in vivo* localised MR spectroscopy took 25 min. We performed all measurements, including shimming and water suppression calibration, in a single, uninterrupted session of a total duration of approx. 2 hours.

We performed the DTI reconstruction of the data and volumetry using DSI Studio (May 18 2019 build for Windows x64, http://dsi-studio.labsolver.org). DSI Studio uses a linear least-squares fit to the Stejskal-Tanner equation on a pixel-by-pixel basis in DTI reconstruction to calculate the diffusion tensor [30], [31]. Colour-coded, FA, RD, MD and AD maps of the diffusion tensor were generated. The diffusion non-weighted images (b = 0) were extracted from the DTI datasets and used for *in vivo* volumetry. Fig. 1(b) shows an example of a colour-coded map of the diffusion tensor reconstructed from the isometric *in vivo* DTI FSEMS image used to determine the location of the splenium of the corpus callosum (CC).

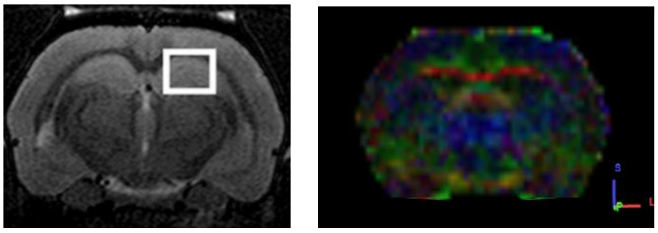

(a) (b)

Fig. 1. (a) T_2-weighted FSEMS axial images for positioning of voxel for localised *in vivo* ^{1}H MRS; (b) colour-coded map of the diffusion tensor, axial section through corpus callosum.

Regions of interest (ROI) for *in vivo* volumetry were manually drawn in both hippocampi and telencephalon by a blinded, expert observer using the DSI Studio ROI tool viewed on the remotely connected, touch-sensitive Android tablet (androidVNC 0.6.0) with the help of the sectional brain atlas [32].

We used colour-coded diffusion tensor maps to assess artefacts. Diffusion non-weighted images (b = 0) were used to assess the signal-to-noise ratio. Low-quality data were rejected (threshold SNR_{b0} = 10). Regions of interest in the caudal part of the CC in the brain midline (splenium), regions in the frontal grey matter (69 mm^3) and regions bilaterally in the temporal grey matter caudal to the splenium (8.6 mm^3) were manually drawn for each animal (Fig. 2).

Tractographies of both cinguli for each animal were then reconstructed using a deterministic tracking algorithm [33] limited to a maximum of 100 tracts for each cingulum (Fig. 2). We set the bifrontal volume as the subvoxel seeding region and the temporal regions as the ROI and region of avoidance (ROA) alternately for the left and right sides. FA threshold was set to a maximum of 0.2, the angular threshold to a maximum of 35°, the step size was equal to half the in-plane resolution, the smoothing parameter was set to 0.2 and the minimum tract length was set to 6 mm. We applied topology-informed pruning with two iterations to remove false connections in reconstructed tracts [34]. We deleted

repeated tracts in the distance of 5 px using DSI Studio's built-in function. We used the same method to reconstruct commissural tracts connecting temporal lobes - forceps maior, with the left region set as the seeding area and the right region set as the ROI (Fig. 2). All reconstructed tracts for each animal were visually inspected by the radiologist to look for false connections and select the best tractographic reconstruction in accordance with the atlas [35].

We cropped the reconstructed tracts to ant, mid, inf and CC ROIs based on the relative position to ROI splenium marked individually for each animal in the previous step (ROI ant: 3 to 5 px rostral to the splenium, size 0.6 mm on the y-axis; ROI mid: 0 to 2 px caudal to the splenium, size 0.6 mm on the y-axis; ROI inf: 0 to 2 px ventral to the splenium, size 0.6 mm on the z-axis; ROI CC: ±1 px on the midline, size 0.6 mm on the x-axis). We exported and summarised the mean values of the measured FA, AD, RD, MD in all DTI ROIs. Right-side ROIs are visualised in Fig. 2.

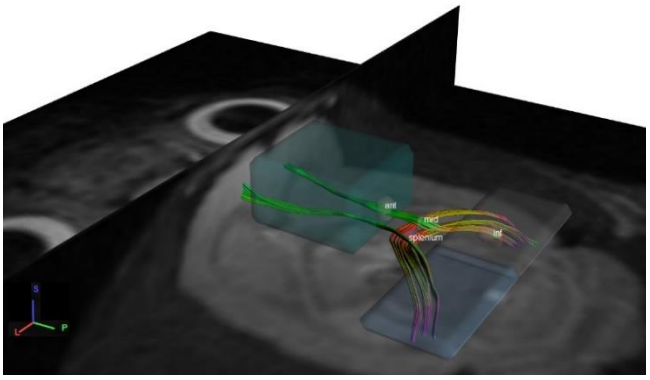

Fig. 2. Rendering of *in vivo* MRI tractography of both cinguli and forceps maior with corresponding start and end regions (boxes), selected regions of interest in the right cingulum (ovals and text).

The second method of DTI data analysis we used was an analysis based on ROIs in the Waxholm Space atlas v4 [36]. The three-dimensional DTI images were registered with the atlas (ITK-SNAP 4.0) [37], transformed (ANTs, built with anaconda v2.4.4) [38] and overlaid with an atlas to allow calculation of mean values (MRtrix3) [39] of diffusion parameters from previously exported parametric maps in selected ROIs in the cingulum, amygdala, basal ganglia, hippocampus, corpus callosum, insula, olfactory bulb, orbitofrontal cortex and white matter tracts.

Due to the different positions of the individual loops of the two-channel receiver coil and the B_0 drift, we corrected the phase and frequency shift of the measured stack of spectra. The processed blocks of spectra were then summed and corrected for eddy currents using non-water-suppressed spectra (VnmrJ). The processed *in vivo* ^{1}H MR spectra from the right hippocampus were quantified using LCModel software [40] (Version 6.3-1). A standard 18-metabolite basis set with built-in spline estimation of the macromolecule baseline was used to deconvolute the spectra in the frequency domain. No correction for T_1 and T_2 relaxation was applied as long TR and short TE were used in the sequence. Metabolite values with Cramér-Rao lower bounds (CRLBs) > 20 % were excluded from further analysis. The following metabolites could be reliably quantified with the LCModel:

- N-acetylaspartate (NAA),
- glutamate (Glu),
- glutamine (Gln),
- taurine (Tau),
- myo-inositol (mIns),
- total creatine (tCr) – creatine (Cr) and phosphocreatine (PCr),
- total choline (tCho) – mainly glycerophosphocholine (GPC) and phosphocholine (PCh) with minor contributions from free choline (Cho) and acetylcholine.

Most metabolites had average CRLBs of less than 10%, with the exception of Gln (13% to 16%) and γ-Aminobutyric acid (GABA) (16% to 22%). The absolute and relative concentrations of the metabolites NAA, Tau, mIns, tCho, Cr, PCr, Glu, Glu+Gln were summarised.

Statistics

Multivariate analysis was performed using SIMCA v. 17 software (Sartorius Stedim Data Analytics AB, Umea, Sweden). Data were standardized to z-scores before proceeding. To explore the sample distribution without classification, the principal component analysis (PCA) was used. Hotelling's T^2 and DmodX tests were applied to identify potential outliers. Subsequently, the Orthogonal projection to Latent Structures Discriminant Analysis (OPLS-DA) was employed. Baseline vs. second measurement relative concentrations of seven metabolites and the relative hippocampal volume were compared for each group. To distinguish between-group differences, the scores plot and the loadings plot were evaluated. The variance (R^2x, R^2y) and predictive ability (Q^2) were established. Generally, values ≥ 0.5 are considered acceptable in biomedical studies; those < 0.5 are classified as poorly describing the model. The VIP plot was used to designate the Variables Important for the Projection, i.e. the independent variables carrying highly discriminating power. Those with a VIP value ≥ 1 are generally considered as significantly contributing to the between-group separation. In addition, a permutation test ($n = 50$) was performed to validate the model. The criterion for validity was that the regression line of the Q^2 intersected the vertical axis at or below zero ($Q^2 \leq 0$).

3. RESULTS

Although the PCA and Hotelling's T^2 tests did not reveal any outliers in the control or HupA groups, the OPLS-DA model failed to identify significant differences between baseline data and second measurement data (data not presented).

As with the D-Gal group, the PCA and Hotelling's T^2 test identified the presence of a partial outlier (at the edge of Hotelling's T^2 tolerance ellipse in Fig. 3), while the DmodX test did not identify any outlier that may affect the model (data not shown); thus, all samples were used for subsequent analyses. The OPLS-DA (Fig. 3, the scores plot) identified a differential distribution of the baseline (Dgal0) and the second measurement samples (Dgal1), the scores are

orthogonal (= completely independent of each other) and represent new variables – the summarised information of all independent variables (herein the relative amounts of seven metabolites and the relative hippocampal volume), so that one score vector corresponds to one animal, having its own score vector. The model shows a partial overlap of the baseline and the second measurement samples (separation in the x-axis direction). The separation in the direction of the y-axis represents within-group variability (Fig. 3). The model described the variance in R^2X and R^2Y satisfactorily (0.55 and 0.65, respectively), but its predictability was low (Q^2 = 0.42). The permutation test results (Q^2: (0.0; -0.927)) showed that the model was not overfitting, confirming its accuracy.

The loadings plot of the model (Fig. 4) shows the relationship between the various independent x variables (green dots) and their association with the dummy variables y (blue dots) representing the baseline (Dgal0) and the second measurement samples (Dgal1). Horizontally, the dummy variables are arranged according to the grouping of scores in the direction of the x-axis in Fig. 3. Independent variables (green dots) adjacent to dummy variables Dgal0 or Dgal1 represent the components with the highest discriminatory power determining the separation between groups; those in the vicinity of Dgal0 are higher in the baseline samples; those adjacent to Dgal1 are higher in the second measurements. Variables positioned near to intersect are similar before and after treatment and, therefore, do not contribute to between-group separation.

The plot of variables of importance (Fig. 5) showed that relative hippocampal volume was the major variable contributing to the separation between groups, with VIP value = 1.62, followed by the relative concentrations of Tau (relTAU) and mIns (relMINS) levels (VIP = 1.14 and VIP = 1.05, respectively). At baseline, the rats showed a higher relative hippocampal volume and a higher relative Tau concentration than in the second measurements, while the relative concentration of mIns showed an opposite direction. VIP values for the remaining variables (relative concentrations of Glu, Gln+Glu, Gln, NAA and tCho) ranged between 0.95 and 0.45. The VIP plot in Fig. 5 shows that the variables adjacent to the origin in the loading scatter plot (Fig. 4) do not contribute significantly to group separation.

Abbreviations used in Fig. 4 and Fig. 5:

- volHipp – relative volume of both hippocampi,
- relTAU – relative concentration of Tau,
- relMINS – relative concentration of mIns,
- relGLU – relative concentration of Glu,
- relGLU/GLN – relative concentration of Glu and Gln,
- relGLN – relative concentration of Gln,
- relNAA – relative concentration of NAA,
- relCHO – relative concentration of Cho,
- DA – discriminant analysis,
- SM10 – subgroup in the 10th model executed within the SIMCA analyses, automatic coding of the software that cannot be deleted or changed by the user.

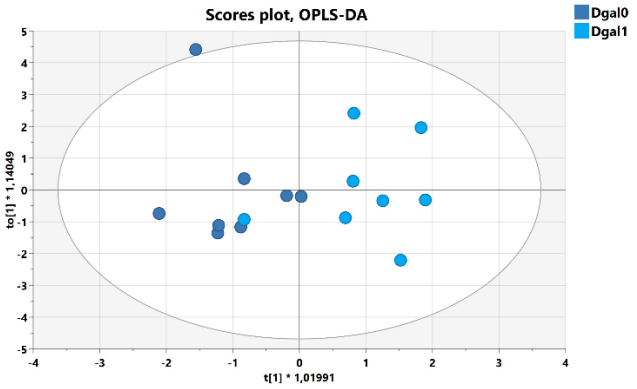

Fig. 3. The multivariate statistical model by OPLS-DA, the score scatter plot of the baseline (Dgal0) and second measurement samples (Dgal1) in rats of the D-Gal group.

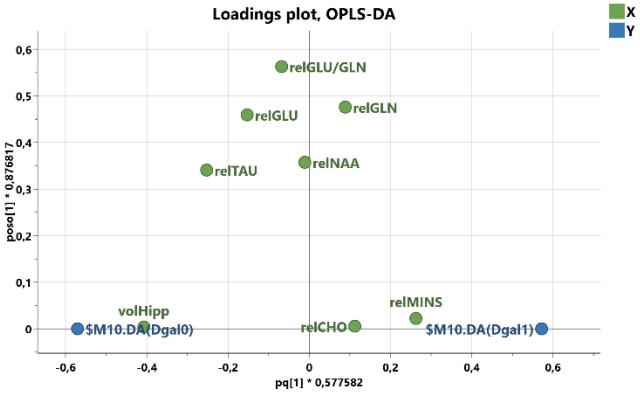

Fig. 4. The loading scatter plot, dummy variables (blue) characterise Dgal0 and Dgal1 samplings in the D-Gal group, pq[1] and poso[1]: predictive and orthogonal component loadings.

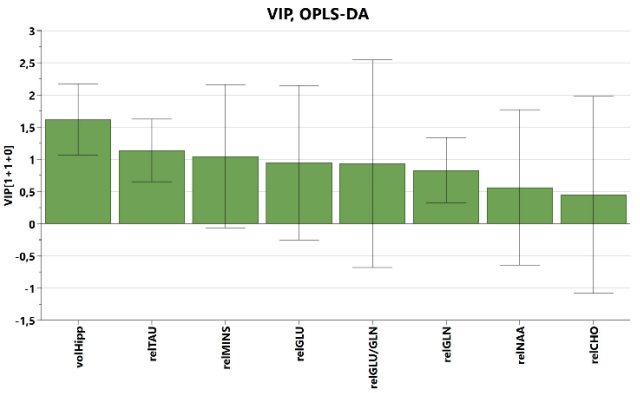

Fig. 5. The plot of VIP contributing to the separation between the baseline and second measurement data (D-Gal group), VIP values in descending order, confidence intervals derived from jack-knifing.

The numerical values of the measured DTI parameters derived from segmentation of the cinguli and registration to the Waxholm Space atlas, the relative hippocampal volumes and the relative concentrations of Tau, mIns in the right hippocampus for the baseline and second measurements are summarised in Table 1 (mean values ±1 standard deviation, the values were rounded to 2 decimal places).

Table 1. DTI, volumetric and selected spectroscopic parameters of the baseline and second measurements (2nd meas.).

	baseline control	baseline D-Gal	baseline DGal+HupA	2nd meas. control	2nd meas. D-Gal	2nd meas. DGal+HupA
FA cingulum	0.27±0.04	0.25±0.05	0.26±0.05	0.30±0.09	0.28±0.04	0.26±0.03
FA amygdala	0.32±0.03	0.31±0.02	0.32±0.02	0.34±0.04	0.29±0.10	0.29±0.07
FA basal ganglia	0.33±0.04	0.31±0.02	0.32±0.04	0.32±0.05	0.32±0.04	0.32±0.02
FA hippocampus	0.30±0.04	0.28±0.02	0.29±0.05	0.30±0.05	0.31±0.04	0.30±0.02
FA brainstem	0.29±0.04	0.23±0.04	0.29±0.04	0.26±0.05	0.22±0.09	0.20±0.06
FA corpus callosum	0.36±0.02	0.31±0.03	0.32±0.04	0.35±0.05	0.34±0.03	0.35±0.02
FA insula	0.28±0.04	0.26±0.03	0.27±0.04	0.28±0.06	0.27±0.03	0.27±0.02
FA olfactory bulb	0.35±0.02	0.34±0.02	0.35±0.04	0.32±0.05	0.34±0.02	0.35±0.03
FA orbitofrontal cortex	0.29±0.06	0.29±0.03	0.30±0.07	0.28±0.05	0.29±0.04	0.28±0.03
FA white matter tracts	0.30±0.02	0.27±0.05	0.29±0.03	0.31±0.02	0.27±0.04	0.26±0.03
FA ROI ant	0.36±0.03	0.33±0.04	0.35±0.06	0.37±0.06	0.36±0.05	0.36±0.07
FA ROI mid	0.43±0.06	0.40±0.04	0.42±0.07	0.40±0.07	0.44±0.04	0.45±0.07
FA ROI inf	0.34±0.05	0.34±0.09	0.31±0.06	0.31±0.05	0.34±0.06	0.33±0.10
MD cingulum [10^{-3}.mm^2.s^{-1}]	0.84±0.08	0.80±0.04	0.82±0.10	0.82±0.09	0.81±0.04	0.82±0.04
MD amygdala [10^{-3}.mm^2.s^{-1}]	0.90±0.08	0,81±0,06	0.86±0.09	0.84±0.10	0.78±0.10	0.75±0.11
MD basal ganglia [10^{-3}.mm^2.s^{-1}]	0.84±0.07	0.79±0.04	0.81±0.10	0.80±0.08	0.79±0.04	0.81±0.04
MD hippocampus [10^{-3}.mm^2.s^{-1}]	0.88±0.09	0.83±0.05	0.85±0.09	0.85±0.10	0.84±0.05	0.85±0.04
MD brainstem [10^{-3}.mm^2.s^{-1}]	0.70±0.10	0.51±0.09	0.64±0.05	0.55±0.13	0.42±0.17	0.43±0.14
MD corpus callosum [10^{-3}.mm^2.s^{-1}]	0.84±0.08	0.80±0.05	0.82±0.09	0.81±0.09	0.81±0.05	0.83±0.05
MD insula [10^{-3}.mm^2.s^{-1}]	0.82±0.07	0.79±0.04	0.80±0.09	0.81±0.07	0.78±0.03	0.80±0.04
MD olfactory bulb [10^{-3}.mm^2.s^{-1}]	0.83±0.06	0.80±0.03	0.82±0.09	0.81±0.07	0.78±0.05	0.81±0.03
MD orbitofrontal cortex [10^{-3}.mm^2.s^{-1}]	0.84±0.07	0.82±0.04	0.83±0.10	0.81±0.08	0.79±0.03	0.81±0.03
MD white matter tracts [10^{-3}.mm^2.s^{-1}]	0.71±0.07	0.62±0.05	0.68±0.08	0.64±0.07	0.60±0.08	0.59±0.06
MD ROI ant [10^{-3}.mm^2.s^{-1}]	0.84±0.11	0.80±0.06	0.76±0.05	0.79±0.07	0.80±0.05	0.83±0.07
MD ROI mid [10^{-3}.mm^2.s^{-1}]	0.80±0.10	0.79±0.04	0.77±0.04	0.79±0.06	0.75±0.05	0.77±0.08
MD ROI inf [10^{-3}.mm^2.s^{-1}]	0.89±0.16	0.85±0.14	0.77±0.03	0.88±0.15	0.80±0.05	0.92±0.14
RD cingulum [10^{-3}.mm^2.s^{-1}]	0.73±0.05	0.70±0.02	0.71±0.06	0.69±0.05	0.69±0.02	0.70±0.02
RD amygdala [10^{-3}.mm^2.s^{-1}]	0.74±0.06	0.67±0.06	0.72±0.07	0.67±0.07	0.57±0.17	0.61±0.12
RD basal ganglia [10^{-3}.mm^2.s^{-1}]	0.69±0.04	0.66±0.02	0.67±0.06	0.66±0.04	0.65±0.02	0.67±0.02
RD hippocampus [10^{-3}.mm^2.s^{-1}]	0.74±0.06	0.71±0.03	0.72±0.06	0.71±0.06	0.70±0,02	0.72±0.03
RD brainstem [10^{-3}.mm^2.s^{-1}]	0.56±0.08	0.40±0.08	0.50±0.03	0.39±0.10	0.30±0.14	0.31±0.12
RD corpus callosum [10^{-3}.mm^2.s^{-1}]	0.68±0.06	0.65±0.03	0.66±0.06	0.65±0.06	0.65±0.03	0.67±0.05
RD insula [10^{-3}.mm^2.s^{-1}]	0.70±0.04	0.68±0.03	0.68±0.03	0.68±0.04	0.66±0.01	0.68±0.02
RD olfactory bulb [10^{-3}.mm^2.s^{-1}]	0.68±0.04	0.65±0.01	0.66±0.05	0.66±0.03	0.64±0.01	0.65±0.02
RD orbitofrontal cortex [10^{-3}.mm^2.s^{-1}]	0.71±0.04	0.71±0.02	0.71±0.05	0.70±0.04	0.68±0.02	0.69±0.01
RD white matter tracts [10^{-3}.mm^2.s^{-1}]	0.56±0.05	0.50±0.04	0.53±0.05	0.48±0.05	0.45±0.06	0.45±0.05
RD ROI ant [10^{-3}.mm^2.s^{-1}]	0.67±0.11	0.65±0.05	0.61±0.05	0.62±0.07	0.63±0.07	0.67±0.08
RD ROI mid [10^{-3}.mm^2.s^{-1}]	0.60±0.12	0.61±0.04	0.58±0.05	0.62±0.07	0.56±0.05	0.57±0.10
RD ROI inf [10^{-3}.mm^2.s^{-1}]	0.72±0.14	0.68±0.10	0.64±0.05	0.73±0.10	0.66±0.07	0.76±0.13
AD cingulum [10^{-3}.mm^2.s^{-1}]	1.09±0.12	1.01±0.10	1.04±0.19	1.05±0.16	1.02±0.08	1.04±0.09
AD amygdala [10^{-3}.mm^2.s^{-1}]	1.19±0.14	1,09±0,08	1.16±0.13	1.18±0.14	1.02±0.25	1.06±0.16
AD basal ganglia [10^{-3}.mm^2.s^{-1}]	1.13±0.14	1.04±0.07	1.09±0.18	1.09±0.16	1.05±0.07	1.08±0.08
AD hippocampus [10^{-3}.mm^2.s^{-1}]	1.17±0.15	1.08±0.07	1.12±0.17	1.13±0.19	1.13±0.12	0,99±0,39
AD brainstem [10^{-3}.mm^2.s^{-1}]	1.02±0.13	0.73±0.13	0.94±0.09	0.87±0.16	0.66±0.27	0.65±0.22
AD corpus callosum [10^{-3}.mm^2.s^{-1}]	1.17±0.14	1.09±0.09	1.12±0.17	1.13±0.16	1.13±0.10	1.14±0.06
AD insula [10^{-3}.mm^2.s^{-1}]	1.08±0.13	1.01±0.08	1.05±0.19	1.06±0.16	1.01±0.08	1.04±0.07
AD olfactory bulb [10^{-3}.mm^2.s^{-1}]	1.14±0.09	1.07±0.06	1.12±0.17	1.14±0.13	1.07±0.07	1.11±0.06
AD orbitofrontal cortex [10^{-3}.mm2.s-1]	1.08±0.13	1.03±0.09	1.07±0.21	1.05±0.16	1.02±0.08	1.04±0.07
AD white matter tracts [10^{-3}.mm^2.s^{-1}]	1.04±0.10	0.90±0.09	0.99±0.14	0.96±0.08	0.88±0.11	0.85±0.10
AD ROI ant [10^{-3}.mm^2.s^{-1}]	1.17±0.12	1.09±0.08	1.05±0.09	1.13±0.10	1.14±0.06	1.17±0.10
AD ROI mid [10^{-3}.mm^2.s^{-1}]	1.20±0.06	1.14±0.07	1.15±0.07	1.15±0.09	1.14±0.04	1.17±0.09
AD ROI inf [10^{-3}.mm^2.s^{-1}]	1.23±0.21	1.18±0.25	1.03±0.07	1.18±0.26	1.10±0.07	1.24±0.21
rel. volume of hippocampi [%]	2.76±0.13	3.31±0.16	2.81±0.33	2.65±0.35	2.93±0.20	2.83±0.38
rel. mIns concentration [/tCr]	0.65±0.07	0.61±0.07	0.72±0.06	0.65±0.06	0.68±0.08	0.71±0.04
rel. Tau concentration [/tCr]	0.76±0.08	0.70±0.06	0.74±0.11	0.65±0.06	0.67±0.04	0.69±0.08

4. DISCUSSION

The aim of this study was to find an MRI/MRS biomarker with the best validity for detecting early changes in D-gal simulated neurodegeneration using an experiment in which MR parameters were measured simultaneously during a single anaesthesia. The reason for using multiple modalities in one measurement session is to ensure constant experimental conditions and to limit the effects of anaesthesia on the animal's metabolism [41], in order to compare the validity of modalities mapping the same functional unit in the brain. Measurements in living systems are influenced by a number of independent factors that can affect the evaluation of spectroscopy and imaging.

We evaluated the hippocampal metabolism (^{1}H MRS) and structure (volumetry), white matter from a microstructural point of view (DTI) and followed the changes over time to study the neuroprotective action of HupA.

We used a metabolic model with high subcutaneous doses of D-gal in young male Wistar rats [1], based on brain ageing and possibly neurodegeneration due to chronic oxidative stress and caspase-activated apoptosis [3], [22], [23], [24]. We expected changes similar to those described in people with the sporadic form of Alzheimer's disease [25]. The pathological changes we focused on were the hippocampal neurochemical profile, the atrophy of hippocampi and the changes in the cingulum microstructure.

The total brain volumes of the animals in all groups increased over the course of the experiment. This finding was consistent with the continuous weight gain of all animals over the course of the experiment. We evaluated the relative volume of the hippocampi, easily distinguishable morphological structures whose volume decreases in the early stages of neurodegeneration due to sensitivity to oxidative stress and ageing [42]. The decrease in the relative volume of the hippocampi in the D-gal group is consistent with the asymmetric loss of hippocampal volume in Alzheimer's disease in humans [43]. There was a possible amelioration of D-gal overdose by HupA in group three, Huperzine A could protect the hippocampal region from initial neurodegeneration [3], since the administration of huperzine prevented both the decrease in volume of the hippocampal region and the increase in mIns in this region. Based on volumetric findings only, the basis for the reduction in hippocampal volume may be loss of water in the glial cells, loss of neurons, or any combination of these processes [44].

An increase in the relative concentration of mIns could be one of the earliest changes in Alzheimer's disease. We have not observed a decrease in NAA, which is considered a marker for neuronal functionality and loss of neurons, and accompanies mIns changes in early Alzheimer's disease [45], [46]. An increase in the relative concentration of mIns as an osmotically active molecule could be related to changes in the relative volume of the hippocampus, it is a marker for glial cells, the volumetric change due to loss of neuronal functionality is therefore less likely, we favour water loss in glial cells. Based on these findings, we believe that we have modelled an early stage of neurodegeneration.

We are interested in whether this could be a sensitive early marker for neurodegenerative disease or a biomarker for monitoring disease progression and response to treatment. In Alzheimer's disease, myo-inositol shows promise in the diagnosis of amnestic MCI, a condition in which memory is reduced without overall impairment of cognitive function. Myo-inositol is increased in the hippocampi of patients with Alzheimer's disease, and there is evidence that lower increases in myo-inositol may occur in MCI patients compared to controls [47].

Analysis of the data from DTI showed that, we did not detect statistically significant changes in the microstructural parameters of the white matter functionally associated with the hippocampus in our animal model of the ageing brain. The potential of tractography should not be overestimated. We used DTI tractography to reveal the course of the cinguli on both sides and commissural tracts connecting the temporal lobes (forceps maior). Due to the larger volume of the tracts, manual segmentation using colour-coded diffusion tensor maps is possible in humans [14]. In *in vivo* imaging of small animals, the tracts are ill-defined, so this procedure cannot be used. The images' spatial resolution is limited by the acquisition times. We chose a fast spin-echo sequence instead of the potentially faster echo-planar imaging because of the need for artefact reduction and because of spatial resolution limitation [48]. The number of non-collinear diffusion directions sampled and the half-sphere scheme can be easily adapted to the needs of the experiment. We found the balance between imaging time in the multimodal experiment and a sufficient signal-to-noise ratio. During reconstruction, we tested the parameters of the tracking algorithm for a specific animal individually, visually confirmed the tract's path, and limited the number of repeated tracts to minimise the size of ROI. We suspect that differences in SNR and image quality between animals were caused by random movements and variations in surface coil positioning (variability in subcutaneous fat tissue thickness). To remove singular noisy tracts, we used automatic topology-informed pruning, which did not cause problems with unnecessary removal of fine tracts in our experiment [34]. Therefore, quantitative evaluation of tractography is not possible in our setting [19]. Tractography was successfully reconstructed in measurements with $SNR_{b0} > 10$ as measured in the dorsal part of the right hippocampus. This is in good agreement with the published data [49]. Our DTI measurements were acquired with a b-value equal to 1100 $s.mm^{-2}$, which was determined by testing of maximal signal drop in trace experiments. Higher b-values, as recommended in the literature, would require an even higher SNR, which is a limitation in *in vivo* small animal experiments [49].

Generally accepted changes in pathological processes in the white matter are a decrease in FA with an increase in RD in neurodegenerative processes [16], if reactive gliosis is present, FA and AD could be increased [50]. Some processes are characterised by an increase in MD. Due to the approximation in the DTI model, which does not consider fibre crossing prevalent in most parts of the white matter [18], it is not possible to unambiguously determine the microstructural background of the diffusion changes. The exact cause of the signal drop and the changes in the derived parameters of the DTI is not clear without histological

correlation [19]. We suspect that the measurements were also influenced by the lateral asymmetry of the rat brain. In humans, there was a significant difference in the FA values for the left and right cinguli [16], which could be caused by its morphological asymmetry and influence on tractographic reconstruction. In our experiment, we also detected asymmetry in the tractography, which could be caused by the lateralisation of rat brain hemispheres. Since the reconstruction of the tracts was limited by a finite number of seed points and the reconstructed tract bundles were slimmed down to achieve a uniform ROI volume, we cannot compare the tract densities.

We assumed that the metabolic changes measurable by localized spectroscopy would not show significant side differences, so we chose measurements in the right hippocampus only. According to the literature, bilateral ^{1}H MRS in brain pathological models did not show significant side differences or showed significant results only – on the right side [51], [52]. In bilateral MRS measurements, apart from the measurement time, the other side would require new shimming and water signal suppression calibration.

We found no significant changes in the measured metabolic, volumetric or diffusion parameters in the control group over time.

In studies using pathophysiological and transgenic models of neurodegeneration at different developmental stages, metabolic changes in the brain were found to manifest earlier than volumetric changes [53]. In our multimodal study, the hippocampal volumetric changes in the D-gal group proved to be the parameter with the best validity. This suggests that the early stages of modelled ageing manifest only in the hippocampus and that the inflammatory processes in the white matter manifest afterwards. This assumption would be consistent with our findings, as we did not observe any significant changes in FA. We could not detect any change in the concentration of NAA, which is considered a marker for neuronal functionality, and a decrease in the NAA levels occurs in advanced Alzheimer's disease [54], [55], which is also related to a decrease in the volume of the hippocampal region of the brain. In our study, we observed the reduction of the hippocampal region without the reduction in NAA concentration in the measured part of this region, but an increase in mIns was observed. Myo-Inositol is often referred to in the literature as a marker for the early stages of AD in human medicine [56]. It is impossible to determine the cause of the slight loss of volume of the hippocampus from our data. One possible explanation is the loss of water in the brain tissue in the D-Gal group. If this is the case, we would not observe changes in metabolites (decrease in relative concentrations of NAA and Glu/Gln), which are to be expected in AD.

It is clear that the D-Gal metabolic model has limitations depending on the application scheme used [1], [57], [58]. The neuroprotective effect of HupA that we expected was confirmed in this experiment, as we administered this drug from the beginning of the experiment. In contrast to our previous study, where we found that the administration of HupA in the D-Gal model is strongly dependent on the application scheme and may even be harmful to the already ongoing neurodegeneration [58].

5. CONCLUSION

We have developed an MRI/^{1}H MRS protocol for simultaneous *in vivo* measurement of several metabolic, macrostructural and microstructural markers for use in small animal models of brain pathology to ensure unaltered conditions for repeatable non-invasive experiments. In the D-Gal model of "age-related dementia" used in our multimodal experiment, the volumetric and spectroscopic parameters proved to be valid "biomarkers" of simulated "neurodegeneration", even with response to the applied HupA therapy. Changes in diffusion parameters measured in the white matter functionally associated with hippocampi could not be detected, possibly due to the limited effect of D-Gal on brain metabolism.

ACKNOWLEDGMENT

This work was financially supported by the Ministry of Education, science, research and sport of the Slovak Republic (grant VEGA 1/0415/16, APVV–21-0299).

REFERENCES

[1] Sadigh-Eteghad, S., Majdi, A., McCann, S. K., Mahmoudi, J., Vafaee, M. S., Macleod, M. R. (2017). Correction: D-galactose-induced brain ageing model: A systematic review and meta-analysis on cognitive outcomes and oxidative stress indices. *PloS One*, 12 (12), e0190328. https://doi.org/10.1371/journal.pone.0190328

[2] Damar, U., Gersner, R., Johnstone, J. T., Schachter, S., Rotenberg, A. (2016). Huperzine A as a neuroprotective and antiepileptic drug: A review of preclinical research. *Expert Review of Neurotherapeutics*, 16 (6), 671-680. https://doi.org/10.1080/14737175.2016.1175303

[3] Ruan, Q., Hu, X., Ao, H., Ma, H., Gao, Z., Liu, F., Kong, D., Bao, Z., Yu, Z. (2014). The neurovascular protective effects of huperzine A on D-galactose-induced inflammatory damage in the rat hippocampus. *Gerontology*, 60 (5), 424-439. https://doi.org/10.1159/000358235

[4] Prince, M., Bryce, R., Albanese, E., Wimo, A., Ribeiro, W., Ferri, C. P. (2013). The global prevalence of dementia: A systematic review and metaanalysis. *Alzheimer's & Dementia*, 9 (1), 63-75.e2. https://doi.org/10.1016/j.jalz.2012.11.007

[5] Hort, J., O'Brien, J. T., Gainotti, G., Pirttila, T., Popescu, B. O., Rektorova, I., Sorbi, S., Scheltens, P. (2010). EFNS guidelines for the diagnosis and management of Alzheimer's disease. *European Journal of Neurology*, 17 (10), 1236-1248. https://doi.org/10.1111/j.1468-1331.2010.03040.x

[6] Schroeter, M. L., Stein, T., Maslowski, N., Neumann, J. (2009). Neural correlates of Alzheimer's disease and mild cognitive impairment: A systematic and quantitative meta-analysis involving 1351 patients. *Neuroimage*, 47 (4), 1196-1206. https://doi.org/10.1016/j.neuroimage.2009.05.037

[7] Wattjes, M. P., Henneman, W. J., van der Flier, W. M., de Vries, O., Träber, F., Geurts, J. J., Scheltens, P., Vrenken, H., Barkhof, F. (2009). Diagnostic imaging of patients in a memory clinic: Comparison of MR imaging and 64-detector row CT. *Radiology*, 253 (1), 174-183. https://doi.org/10.1148/radiol.2531082262

[8] Wahlund, L.-O., Julin, P., Johansson, S.-E., Scheltens, P. (2000). Visual rating and volumetry of the medial temporal lobe on magnetic resonance imaging in dementia: a comparative study. *Journal of Neurology, Neurosurgery & Psychiatry*, 69 (5), 630-635. http://dx.doi.org/10.1136/jnnp.69.5.630

[9] O'Brien, J. T. (2007). Role of imaging techniques in the diagnosis of dementia. *The British Journal of Radiology*, 80 (special_issue_2), S71-S77. https://doi.org/10.1259/bjr/33117326

[10] Patel, K. P., Wymer, D. T., Bhatia, V. K., Duara, R., Rajadhyaksha, C. D. (2020). Multimodality imaging of dementia: Clinical importance and role of integrated anatomic and molecular imaging. *RadioGraphics*, 40 (1), 200-222. https://doi.org/10.1148/rg.2020190070

[11] Loos, C., Achten, E., Santens, P. (2010). Proton magnetic resonance spectroscopy in Alzheimer's disease, a review. *Acta Neurologica Belgica*, 110 (4), 291-298. https://www.actaneurologica.be/pdfs/2010-4/01-Loos et al.pdf

[12] Waller, A. (1850). Experiments on the frog, and observations of the alterations produced thereby in the structure of their primitive fibers. *Philosophical Transactions of the Royal Society of London, Series B: Biological Sciences*, 140, 423-429.

[13] Amlien, I. K., Fjell, A. M. (2014). Diffusion tensor imaging of white matter degeneration in Alzheimer's disease and mild cognitive impairment. *Neuroscience*, 276, 206-215. https://doi.org/10.1016/j.neuroscience.2014.02.017

[14] Delano-Wood, L., Stricker, N. H., Sorg, S. F., Nation, D. A., Jak, A. J., Woods, S. P., Libon, D. J., Delis, D. C., Frank, L. R., Bondi, M. W. (2012). Posterior cingulum white matter disruption and its associations with verbal memory and stroke risk in mild cognitive impairment. *Journal of Alzheimer's Disease*, 29 (3), 589-603. https://doi.org/10.3233/JAD-2012-102103

[15] Head, D., Buckner, R. L., Shimony, J. S., Williams, L. E., Akbudak, E., Conturo, T. E., McAvoy, M., Morris, J. C., Snyder, A. Z. (2004). Differential vulnerability of anterior white matter in nondemented aging with minimal acceleration in dementia of the Alzheimer type: Evidence from diffusion tensor imaging. *Cerebral Cortex*, 14 (4), 410-423. https://doi.org/10.1093/cercor/bhh003

[16] Catheline, G., Periot, O., Amirault, M., Braun, M., Dartigues, J.-F., Auriacombe, S., Allard, M. (2010). Distinctive alterations of the cingulum bundle during aging and Alzheimer's disease. *Neurobiology of Aging*, 31 (9), 1582-1592. https://doi.org/10.1016/j.neurobiolaging.2008.08.012

[17] Basser, P. J. (1995). Inferring microstructural features and the physiological state of tissues from diffusion-weighted images. *NMR in Biomedicine*, 8 (7), 333-344. https://doi.org/10.1002/nbm.1940080707

[18] Jeurissen, B., Leemans, A., Tournier, J.-D., Jones, D. K., Sijbers, J. (2013). Investigating the prevalence of complex fiber configurations in white matter tissue with diffusion magnetic resonance imaging. *Human Brain Mapping*, 34 (11), 2747-2766. https://doi.org/10.1002/hbm.22099

[19] Jones, D. K., Knösche, T. R., Turner, R. (2013). White matter integrity, fiber count, and other fallacies: The do's and don'ts of diffusion MRI. *Neuroimage*, 73, 239-254. https://doi.org/10.1016/j.neuroimage.2012.06.081

[20] Foster, T. C. (2006). Biological markers of age-related memory deficits. *CNS Drugs*, 20 (2), 153-166. https://doi.org/10.2165/00023210-200620020-00006

[21] Holden, H. M., Rayment, I., Thoden, J. B. (2003). Structure and function of enzymes of the Leloir pathway for galactose metabolism. *Journal of Biological Chemistry*, 278 (45), 43885-43888. https://doi.org/10.1074/jbc.R300025200

[22] Song, X. U., Bao, M., Li, D., Li, Y. M. (1999). Advanced glycation in D-galactose induced mouse aging model. *Mechanisms of Ageing and Development*, 108 (3), 239-251. https://doi.org/10.1016/S0047-6374(99)00022-6

[23] Gasparotto, J., Girardi, C. S., Somensi, N., Ribeiro, C. T., Moreira, J. C., Michels, M., Sonai, B., Rocha, M., Steckert, A. V., Barichello, T., Quevedo, J., Dal-Pizzol, F., Gelain, D. P. (2018). Receptor for advanced glycation end products mediates sepsis-triggered amyloid-β accumulation, Tau phosphorylation, and cognitive impairment. *Journal of Biological Chemistry*, 293 (1), 226-244. https://doi.org/10.1074/jbc.M117.786756

[24] Tobon-Velasco, J. C., Cuevas, E., Torres-Ramos, M. A. (2014). Receptor for AGEs (RAGE) as mediator of NF-kB pathway activation in neuroinflammation and oxidative stress. *CNS & Neurological Disorders: Drug Targets*, 13 (9), 1615-1626. http://dx.doi.org/10.2174/1871527313666140806144831

[25] Hua, X., Lei, M., Zhang, Y., Ding, J., Han, Q., Hu, G., Xiao, M. (2007). Long-term D-galactose injection combined with ovariectomy serves as a new rodent model for Alzheimer's disease. *Life Sciences*, 80 (20), 1897-1905. https://doi.org/10.1016/j.lfs.2007.02.030

[26] Schmidt, R., Hofer, E., Bouwman, F. H., Buerger, K., Cordonnier, C., Fladby, T., Galimberti, D., Georges, J., Heneka, M. T., Hort, J., Laczó, J., Molinuevo, J. L., O'Brien, J. T., Religa, D., Scheltens, P., Schott, J. M., Sorbi, S. (2015). EFNS-ENS/EAN Guideline on concomitant use of cholinesterase inhibitors and memantine in moderate to severe Alzheimer's disease. *European Journal of Neurology*, 22 (6), 889-898. https://doi.org/10.1111/ene.12707

[27] Gruetter, R. (1993). Automatic, localized *in Vivo* adjustment of all first-and second-order shim coils. *Magnetic Resonance in Medicine*, 29 (6), 804-811. https://doi.org/10.1002/mrm.1910290613

[28] Tkáč, I., Starčuk, Z., Choi, I.-Y., Gruetter, R. (1999). In vivo ^{1}H NMR spectroscopy of rat brain at 1 ms echo time. *Magnetic Resonance in Medicine*, 41, 649-656. https://doi.org/10.1002/(SICI)1522-2594(199904)41:4%3C649::AID-MRM2%3E3.0.CO;2-G

[29] Mlynárik, V., Gambarota, G., Frenkel, H., Gruetter, R. (2006). Localized short-echo-time proton MR spectroscopy with full signal-intensity acquisition. *Magnetic Resonance in Medicine*, 56 (5), 965-970. https://doi.org/10.1002/mrm.21043

[30] Basser, P. J., Mattiello, J., Lebihan, D. (1994). Estimation of the effective self-diffusion tensor from the NMR spin echo. *Journal of Magnetic Resonance, Series B*, 103 (3), 247-254.

[31] Jiang, H., Van Zijl, P. C., Kim, J., Pearlson, G. D., Mori, S. (2006). DtiStudio: Resource program for diffusion tensor computation and fiber bundle tracking. *Computer Methods and Programs in Biomedicine*, 81 (2), 106-116. https://doi.org/10.1016/j.cmpb.2005.08.004

[32] Paxinos, G., Watson, C. (2007). *The Rat Brain in Stereotaxic Coordinates*. Elsevier, ISBN 978-0-12-547620-1.

[33] Yeh, F.-C., Verstynen, T. D., Wang, Y., Fernández-Miranda, J. C., Tseng, W.-Y. I. (2013). Deterministic diffusion fiber tracking improved by quantitative anisotropy. *PloS One*, 8 (11). https://doi.org/10.1371/journal.pone.0080713

[34] Yeh, F.-C., Panesar, S., Barrios, J., Fernandes, D., Abhinav, K., Meola, A., Fernandez-Miranda, J. C. (2019). Automatic removal of false connections in diffusion mri tractography using topology-informed pruning (TIP). *Neurotherapeutics*, 16 (1), 52-58. https://doi.org/10.1007/s13311-018-0663-y

[35] Veraart, J., Leergaard, T. B., Antonsen, B. T., Van Hecke, W., Blockx, I., Jeurissen, B., Jiang, Y., Van der Linden, A., Johnson, G. A., Verhoye, M., Sijbers, J. (2011). Population-averaged diffusion tensor imaging atlas of the Sprague Dawley rat brain. *Neuroimage*, 58 (4), 975-983. https://doi.org/10.1016/j.neuroimage.2011.06.063

[36] Papp, E. A., Leergaard, T. B., Calabrese, E., Johnson, G. A., Bjaalie, J. G. (2014). Waxholm Space atlas of the Sprague Dawley rat brain. *NeuroImage*, 97, 374-386. https://doi.org/10.1016/j.neuroimage.2014.04.001

[37] Yushkevich, P. A., Piven, J., Hazlett, H. C., Smith, R. G., Ho, S., Gee, J. C., Gerig, G. (2006). User-guided 3D active contour segmentation of anatomical structures: Significantly improved efficiency and reliability. *Neuroimage*, 31 (3), 1116-1128. https://doi.org/10.1016/j.neuroimage.2006.01.015

[38] Pluta, J., Avants, B. B., Glynn, S., Awate, S., Gee, J. C., Detre, J. A. (2009). Appearance and incomplete label matching for diffeomorphic template based hippocampus segmentation. *Hippocampus*, 19 (6), 565-571. https://doi.org/10.1002/hipo.20619

[39] Tournier, J.-D., Smith, R., Raffelt, D., Tabbara, R., Dhollander, T., Pietsch, M., Christiaens, D., Jeurissen, B., Yeh, C.-H., Connelly, A. (2019). *MRtrix3*: A fast, flexible and open software framework for medical image processing and visualisation. *Neuroimage*, 202 116137. https://doi.org/10.1016/j.neuroimage.2019.116137

[40] Provencher, S. W. (1993). Estimation of metabolite concentrations from localized in vivo proton NMR spectra. *Magnetic Resonance in Medicine*, 30 (6), 672-679. https://doi.org/10.1002/mrm.1910300604

[41] Xie, Z., Dong, Y., Maeda, U., Moir, R. D., Xia, W., Culley, D. J., Crosby, G., Tanzi, R. E. (2007). The inhalation anesthetic isoflurane induces a vicious cycle of apoptosis and amyloid β-protein accumulation. *Journal of Neuroscience*, 27 (6), 1247-1254. https://doi.org/10.1523/JNEUROSCI.5320-06.2007

[42] McEwen, B. S. (2007). Physiology and neurobiology of stress and adaptation: Central role of the brain. *Physiological Reviews*, 87 (3), 873-904. https://doi.org/10.1152/physrev.00041.2006

[43] Petersen, R. C., Jack, C. R., Xu, Y.-C., Waring, S. C., O'Brien, P. C., Smith, G. E., Ivnik, R. J., Tangalos, E. G., Boeve, B. F., Kokmen, E. (2000). Memory and MRI-based hippocampal volumes in aging and AD. *Neurology*, 54 (3), 581-581. https://doi.org/10.1212/WNL.54.3.581

[44] Morrison, J. H., Hof, P. R. (1997). Life and death of neurons in the aging brain. *Science*, 278 (5337), 412-419. https://doi.org/10.1126/science.278.5337.412

[45] Voevodskaya, O., Poulakis, K., Sundgren, P., Westen, D. V., Palmqvist, S., Wahlund, L., Stomrud, E., Hansson, O., Westmanet, E. (2019). Brain myoinositol as a potential marker of amyloid-related pathology. *Neurology*, 92 (5). https://doi.org/10.1212/WNL.0000000000006852

[46] Mlynárik, V., Cacquevel, M., Sun-Reimer, L., Janssens, S., Cudalbu, C., Lei, H., Schneider, B. L., Aebischer, P., Gruetteret, R. (2012). Proton and phosphorus magnetic resonance spectroscopy of a mouse model of Alzheimer's disease. *Journal of Alzheimer's Disease*, 31 (s3), S87-S99. https://doi.org/10.3233/jad-2012-112072

[47] Watanabe, T., Shiino, A., Akiguchi, I. (2012). Hippocampal metabolites and memory performances in patients with amnestic mild cognitive impairment and Alzheimer's disease. *Neurobiology of Learning and Memory*, 97 (3), 289-293. https://doi.org/10.1016/j.nlm.2012.01.006

[48] Van Hecke, W., Emsell, L., Sunaert, S. (eds.) (2016). *Diffusion Tensor Imaging: A Practical Handbook*. Springer. https://doi.org/10.1007/978-1-4939-3118-7

[49] Descoteaux, M., Deriche, R., Knosche, T. R., Anwander, A. (2008). Deterministic and probabilistic tractography based on complex fibre orientation distributions. *IEEE Transactions on Medical Imaging*, 28 (2), 269-286. https://doi.org/10.1109/TMI.2008.2004424

[50] Budde, M. D., Janes, L., Gold, E., Turtzo, L. C., Frank, J. A. (2011). The contribution of gliosis to diffusion tensor anisotropy and tractography following traumatic brain injury: Validation in the rat using Fourier analysis of stained tissue sections. *Brain*, 134 (8), 2248-2260. https://doi.org/10.1093/brain/awr161

[51] Xi, G., Hui, J., Zhang, Z., Liu, S., Zhang, X., Teng, G., Chan, K. C., Wu, E. X., Nie, B., Shan, B., Li, L., Reynolds, G. P. (2011). Learning and memory alterations are associated with hippocampal N-acetylaspartate in a rat model of depression as measured by 1H-MRS. *PloS One*, 6 (12), e28686. https://doi.org/10.1371/journal.pone.0028686

[52] Marjanska, M., Curran, G. L., Wengenack, T. M., Henry, P.-G., Bliss, R. L., Poduslo, J. F., Jack Jr, C. R., Ugurbil, K., Garwood, M. (2005). Monitoring disease progression in transgenic mouse models of Alzheimer's disease with proton magnetic resonance spectroscopy. *Proceedings of the National Academy of Sciences*, 102 (33), 11906-11910. https://doi.org/10.1073/pnas.0505513102

[53] Márquez, F., Yassa, M. A. (2019). Neuroimaging biomarkers for Alzheimer's disease. *Molecular Neurodegeneration*, 14 (1), 21. https://doi.org/10.1186/s13024-019-0325-5

[54] Veeraiah, P., Jansen, J. F. (2023). Multinuclear magnetic resonance spectroscopy at ultra-high-field: Assessing human cerebral metabolism in healthy and diseased states. *Metabolites*, 13 (4), 577. https://doi.org/10.3390/metabo13040577

[55] Block, W., Jessen, F., Träber, F., Flacke, S., Manka, C., Lamerichs, R., Keller, E., Heun, R., Schild, H. (2002). Regional N-acetylaspartate reduction in the hippocampus detected with fast proton magnetic resonance spectroscopic imaging in patients with Alzheimer disease. *Archives of Neurology*, 59 (5), 828-834. https://doi.org/10.1001/archneur.59.5.828

[56] Marjańska, M., McCarten, J. R., Hodges, J. S., Hemmy, L. S., Terpstra, M. (2019). Distinctive neurochemistry in Alzheimer's disease via 7 T in vivo magnetic resonance spectroscopy. *Journal of Alzheimer's Disease*, 68 (2), 559-569. https://doi.org/10.3233%2FJAD-180861

[57] Sumbalová, Z., Uličná, O., Kucharská, J., Rausová, Z., Vančová, O., Melicherčík, L., Tvrdík, T., Nemec, M., Kašparová, S. (2022). D-galactose-induced aging in rats - The effect of metformin on bioenergetics of brain, skeletal muscle and liver. *Experimental Gerontology*, 163, 111770. https://doi.org/10.1016/j.exger.2022.111770

[58] Melichercik, L., Tvrdik, T., Novakova, K., Nemec, M., Kalinak, M., Baciak, L., Kasparova, S. (2022). Huperzine aggravated neurochemical and volumetric changes induced by D-galactose in the model of neurodegeneration in rats. *Neurochemistry International*, 158, 105365. https://doi.org/10.1016/j.neuint.2022.105365

Received July 17, 2023
Accepted September 25, 2023